GPMS: Enabling Indoor GNSS Positioning using Passive Metasurfaces

Yezhou Wang[†‡]
Shanghai Jiao Tong University
yezhouwang@sjtu.edu.cn

Hao Pan[*]
Microsoft Research Asia
panhao@microsoft.com

Lili Qiu
Microsoft Research Asia
liliqiu@microsoft.com

Linghui Zhong[†]
Central South University
zlh2021@csu.edu.cn

Jiting Liu[†]
Columbia University
jl6247@columbia.edu

Ruichun Ma
Yale University
ruichun.ma@yale.edu

Yi-Chao Chen[‡]
Shanghai Jiao Tong University
yichao@sjtu.edu.cn

Guangtao Xue[‡]
Shanghai Jiao Tong University
gt_xue@sjtu.edu.cn

Ju Ren
Tsinghua University
renju@tsinghua.edu.cn

ABSTRACT

Global Navigation Satellite System (GNSS) is extensively utilized for outdoor positioning and navigation. However, achieving high-precision indoor positioning is challenging due to the significant attenuation of GNSS signals indoors. To address this issue, we propose an innovative indoor GNSS positioning system called GPMS, which uses passive metasurface technology to redirect GNSS signals from outdoors into indoor spaces. These passive metasurfaces are strategically optimized for indoor coverage by steering and scattering the GNSS signals across a wide range of incident angles. We further develop a novel localization algorithm that can determine which metasurface the signal goes through and localize the user using the set of metasurfaces as anchor points. A distinct advantage of our localization algorithm is that it can be implemented on existing mobile devices without any hardware modifications. We implement the prototype of GPMS, and deploy six metasurfaces in two indoor environments, a 10×50 m^2 office floor and a 15×20 m^2 lecture room, to evaluate system performance. In terms of coverage, our GPMS increases the C/N0 from 9.1 dB-Hz to 23.2 dB-Hz and increases the number of visible satellites from 3.6 to 21.5 in the office floor. In terms of indoor positioning accuracy, our proposed system decreases the absolute positioning error from 30.6 m to 3.2 m in the office floor, and from 11.2 m to 2.7 m in the lecture room, demonstrating the feasibility and benefits of metasurface-assisted GNSS for indoor positioning.

CCS CONCEPTS

• **Information systems** → **Global positioning systems**; • **Hardware** → *Networking hardware*.

KEYWORDS

GNSS system; Indoor positioning; Passive metasurface

ACM Reference Format:
Yezhou Wang, Hao Pan, Lili Qiu, Linghui Zhong, Jiting Liu, Ruichun Ma, Yi-Chao Chen, Guangtao Xue, and Ju Ren. 2024. GPMS: Enabling Indoor GNSS Positioning using Passive Metasurfaces. In *The 30th Annual International Conference on Mobile Computing and Networking (ACM MobiCom '24), November 18–22, 2024, Washington D.C., DC, USA.* ACM, New York, NY, USA, 15 pages. https://doi.org/10.1145/3636534.3690702

1 INTRODUCTION

Global Navigation Satellite System (GNSS) is ubiquitous for outdoor navigation [22]. However, GNSS signals face challenges in penetrating indoor environments, primarily due to signal obstruction, reflection, and attenuation caused by physical barriers [23, 38]. Wi-Fi/Bluetooth Low Energy (BLE) technologies offer potential solutions to indoor positioning, but they face several significant challenges [16, 40]. First,

[*]Hao Pan is the corresponding author
[†]Yezhou Wang, Linghui Zhong, and Jiting Liu did this work as interns at Microsoft Research Asia
[‡]Also with Shanghai Key Laboratory of Trusted Data Circulation and Governance in Web3.

Permission to make digital or hard copies of all or part of this work for personal or classroom use is granted without fee provided that copies are not made or distributed for profit or commercial advantage and that copies bear this notice and the full citation on the first page. Copyrights for components of this work owned by others than the author(s) must be honored. Abstracting with credit is permitted. To copy otherwise, or republish, to post on servers or to redistribute to lists, requires prior specific permission and/or a fee. Request permissions from permissions@acm.org.

ACM MobiCom '24, November 18–22, 2024, Washington D.C., DC, USA

© 2024 Copyright held by the owner/author(s). Publication rights licensed to ACM.

ACM ISBN 979-8-4007-0489-5/24/11…$15.00
https://doi.org/10.1145/3636534.3690702

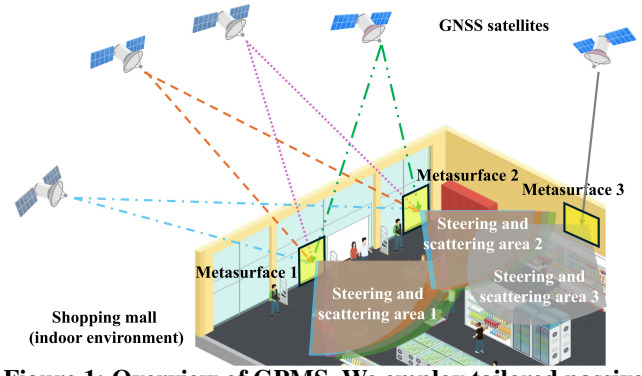

Figure 1: Overview of GPMS. We employ tailored passive metasurfaces to direct GNSS signals indoors, coupled with modified positioning algorithms, enabling accurate indoor localization on mobile devices

they require additional infrastructure and area-specific calibration and ongoing maintenance, which is not only costly but also complicated. Moreover, estimating Angle of Arrival (AoA) for accurate positioning requires a large antenna array and accurate clock synchronization, which further increases costs. Moreover, accurate positioning requires mobile devices support specific hardware and software protocols, such as 802.11mc FTM [9]. Unlike Wi-Fi/BLE solutions, GNSS-based solutions obviate the need for the deployment and maintenance of base stations by leveraging widely available satellites. Moreover, almost all smartphones are equipped with GNSS chips and allow for direct access to GNSS pseudoranges via APIs. Thus, bringing GNSS signals indoors is crucial for accurate ubiquitous indoor positioning.

GPS repeaters [3] are a potential method for indoor GNSS extension, but they introduce variable delays that can lead to location errors and require multiple devices along with corresponding complex calibration to ensure full coverage [12, 42]. Moreover, they demand a continuous power supply for operation. Passive options like GPS backscatter devices provide a similar function to repeaters. GPSMirror [15] proposes a backscatter-based indoor GNSS extension solution. However, the GNSS signal strength captured by the backscatter device is limited by its small antenna aperture, and its output power is also very restricted, making it unable to effectively amplify the signals indoors. Additionally, their positioning algorithm depends on at least two direct Line-of-Sight (LoS) GNSS signals, a condition that is difficult to meet indoors.

Electromagnetic (EM) metasurfaces, with structured arrays to control EM waves, offer a novel and promising approach for extending GNSS indoors. Unlike repeaters, metasurfaces can passively redirect signals without delay or power supply. Metasurfaces have powerful capability in manipulating EM wavefront. Since passive metasurfaces are low-cost and can span considerable areas, they can capture more GNSS signal energy than the limited apertures of backscatter antennas.

To this end, we develop the first system that uses passive metasurfaces to bring GNSS signals indoor and leverages the signals strengthened by multiple metasurfaces for accurate indoor positioning. Our system is called GNSS Positioning Metasurfaces based System (GPMS). As depicted in Figure 1, GPMS utilizes strategically positioned passive metasurfaces on the windows of a building, serving as "signal controllers" to redirect GNSS signals indoors. These metasurfaces enhance signal strength, providing high SNR for indoor GNSS receivers to efficiently decode data and mitigate multipath interference through steering.

Designing passive metasurfaces that can effectively steer and scatter signals from all GNSS satellites within the visible range presents a significant challenge. Passive metasurfaces lack programmability, meaning their wavefront manipulation capabilities are fixed upon fabrication. Therefore, we need to determine a general and robust passive metasurface design that can efficiently (1) steer signals from all visible GNSS satellites at various incident angles in the elevation dimension to guide signals indoors, and (2) scatter these incoming signals in the azimuth dimension to maximize indoor coverage of GNSS signals. This presents a complex problem similar to directing light beams from multiple directions through a lens towards a single direction, which is virtually infeasible with only one lens due to the principle of reversibility of light paths. Inspired by systems using lenses combination, we aim to steer and scatter GNSS signals with varying incident angles through the combination of two metasurfaces. We cast the joint design of two metasurfaces (*e.g.*, their phase maps) as an optimization problem. Considering the dual-frequency nature of GNSS systems, which includes the L1 and L5 bands, we utilize a transmissive meta-atom structure capable of supporting both frequency bands to facilitate the realization of the final metasurface. We optimize the metasurface phase maps for the L1 and L5 bands independently and subsequently integrate them into a unified metasurface assembly system. The resulting metasurface assembly system is capable of steering and scattering dual-frequency GNSS signals to achieve indoor signal coverage.

After metasurfaces redirect GNSS signals indoors, traditional GNSS positioning algorithms cannot correctly locate indoor users due to the addition of the metasurface as an intermediary in the signal path. To achieve accurate indoor positioning, we develop a novel positioning algorithm that treats GNSS metasurfaces as a new anchor to calculates the user's position. By post-processing raw GNSS message data, such as pseudorange, we can identify which metasurfaces relay signals indoors and use their known coordinates to establish geometric equations for calculating the user's position. Note that our algorithm requires no hardware modifications to existing GNSS receivers and chips. We can directly obtain GNSS raw message data through Android APIs [8], which

System	# of satellites	Frequency bands	Bandwidth	Accuracy
GPS [46]	≥ 24	L1 (1575.42 MHz), L2 (1227.60 MHz), L5 (1176.45 MHz)	~20 MHz (L1 C/A)	~5 meters
GLONASS [47]	24	L1 (1602 + k*0.5625 MHz), L2 (1246 + k*0.4375 MHz), k is satellite ID	~2 MHz	5-10 meters
Galileo [45]	~30	E1 (1575.42 MHz), E5a (1176.45 MHz), E5b (1207.14 MHz), E6 (1278.75 MHz)	15-25 MHz (E1 B/C)	~1 meter
BeiDou [44]	≥ 30	B1 (1561.098 MHz), B2 (1207.14 MHz), B3 (1268.52 MHz)	~10 MHz (B1I)	~10 meters

Table 1: Comparison of mainstream GNSS systems

makes it convenient to implement on mobile devices without needing root access.

Our contributions can be summarized as follow:

- To our knowledge, our proposed GPMS is the first GNSS indoor positioning system based on the passive metasurfaces.
- We design an innovative passive metasurface assembly system by combining two metasurfaces, and develop an optimization algorithm to obtain phase map configurations for effective steering and scattering of GNSS signals at various incident angles for a wide indoor coverage.
- We develop an indoor positioning algorithm that can be implemented on a mobile device without hardware modifications. It can identify which metasurface the signal traverses through and use the metasurfaces as new anchors to derive the user's location.
- We implement prototypes of GPMS using six passive metasurfaces in an office floor and a lecture room, respectively. Experiments demonstrate that our metasurfaces can enhance the indoor C/N0 from 9.1 to 23.2 dB-Hz and increase the number of visible satellites from 3.6 to 21.5 in the office floor. Combined with our modified localization algorithm, we achieve an average absolute indoor positioning error of 3.2 m on the office floor and 2.7 m in the lecture room.

2 RELATED WORK

2.1 Existing Indoor Positioning Methods

RF signals: Wi-Fi/BLE has been widely used for indoor localization. Received Signal Strength Indicator (RSSI) based algorithms are easy to implement but incur large errors due to multipath or large variation in signal attenuation across different obstacles. Channel State Information (CSI) fingerprints from multiple beacon devices [11, 13, 16, 17, 19] has been shown to achieve higher accuracy. However, collecting extensive fingerprints is labor-intensive. More recent Wi-Fi/BLE positioning systems leverage AoA information to circumvent extensive data gathering, but they require large antenna arrays and precise clock synchronization in beacon devices, increasing the costs. Moreover, certain Wi-Fi/BLE positioning systems require mobile devices use specific hardware and software protocols, *e.g.*, 802.11mc FTM [9], which limits their deployment. RFID-based methods use phase difference to derive the object's position [24, 26, 28, 50]. Ultra-Wideband (UWB) generates a sharp pulse in the time domain and the Time of Flight (ToF) for localization [39, 56]. However, these methods require deployment of multiple beacons/anchors/tags indoors and synchronization between beacons, which increases deployment cost and complexity.

Visible Light Communication (VLC): Some work employs LED (or other light sources) along with light sensors for localization, typically involving the modulation and demodulation of light signals [51, 55]. However, VLC requires line-of-sight, and its performance degrades in crowded or highly dynamic environments, thus limiting its applicability.

Magnetic Field: The geomagnetic or magnetic field characteristics inside buildings can be utilized as fingerprints for indoor localization [18, 36, 43, 49]. Lu *et al.* [25] and Rallapali [37] both rely on the unique magnetic field characteristics produced by indoor electrical grids to estimate location by analyzing magnetic field variations. However, such localization systems require complex configuration and calibration, and are vulnerable to interference from metal and electronic devices.

Acoustic: Inaudible acoustic signals have been used for localization based on their ToF and AoA [29–32, 53, 54]. However, they require deploying multiple speakers and microphones. Moreover, inaudible acoustic signals have limited sensing range, which increases deployment cost.

Inertial Measurement Unit (IMU): IMU estimates device movement and orientation by combining data from accelerometers, gyroscopes, and magnetometers, as in Pedestrian Dead Reckoning (PDR) [21]. It can further be combined with the aforementioned RF signal-based positioning systems to enhance the accuracy [14, 52].

2.2 Indoor GNSS Positioning

GNSS is widely used for outdoor localization. GNSS use trilateration, where a receiver derives its position by measuring the ToF from at least four satellites and calculating its 3D coordinates and clock bias using the measured distances and the satellites' locations. Positional accuracy in GNSS is affected by factors including SNR, satellite visibility, atmospheric conditions, and multipath. Outdoors tend to have high SNR and dense satellite coverage. Techniques like Differential GNSS (DGNSS), Real-Time Kinematic (RTK), and Wide Area Augmentation System (WAAS) can reduce errors to 1-3 meters. The mainstream GNSS systems are summarized in Table 1.

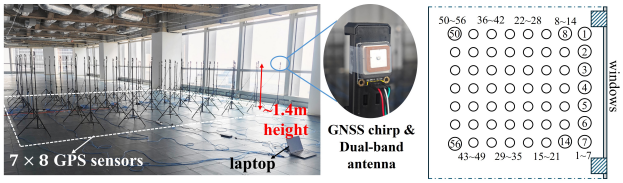

(a) Measurement setup (b) Indoor layout

Figure 2: Experimental setup for measuring indoor GNSS signal quality with a sensor array in an 8×10 m^2 space

Enabling indoor GNSS positioning could deliver a universal solution for both outdoor and indoor environments, offering key benefits, such as a global standard with ubiquitous GNSS chips in mobile devices. This eliminates the need for additional infrastructure, calibration, and updates. Thus, the significant benefits of indoor GNSS have inspired considerable work, including the development of GNSS repeaters and backscatter techniques.

GNSS repeaters: GNSS repeaters use an outdoor antenna to receive GNSS signals, which are then transmitted to an indoor extender antenna unit via a coaxial cable. The primary limitations of GPS repeaters include: (i) they consume watt-level power [15] and require a plug-in supply [15], and (ii) they incur variable processing delay, so precise time synchronization is essential when multiple repeaters are used for covering a large indoor area.

GNSS backscatters: GPSMirror [15] designs a GPS backscatter, which can significantly reduce the power consumption over GNSS repeaters and only need μW level power. However, the approach has the following limitations: (1) it needs power supply; (2) deploying multiple backscatter devices requires clock synchronization for on-off switching, which is complicated; (3) GPSMirror only supports narrowband satellite signals (*e.g.*, L1 band), while the whole bandwidth of GNSS satellite signals is 10 times that of the L1 band; (4) more importantly, GPSMirror requires directly receiving signals from **two or three** satellites, which is hard to realize in indoor scenarios due to obstruction.

2.3 Metasurface for satellite scenarios

Metasurface has attracted an increasing amount of attention in wireless research community due to its powerful wavefront shaping abilities, which enhances signal strength and coverage. We propose the use of passive metasurfaces to enhance GNSS signals in indoor environments without incurring any processing delay. Prior studies, such as PMSat [34], have explored passive metasurface design in Low Earth orbit (LEO) satellite communication scenarios in the Ku- and Ka-bands. Our research differs from PMSat in several critical aspects. (i) PMSat steers the signals towards a target receiver at a known location, whereas this work aims to strengthen GNSS signals

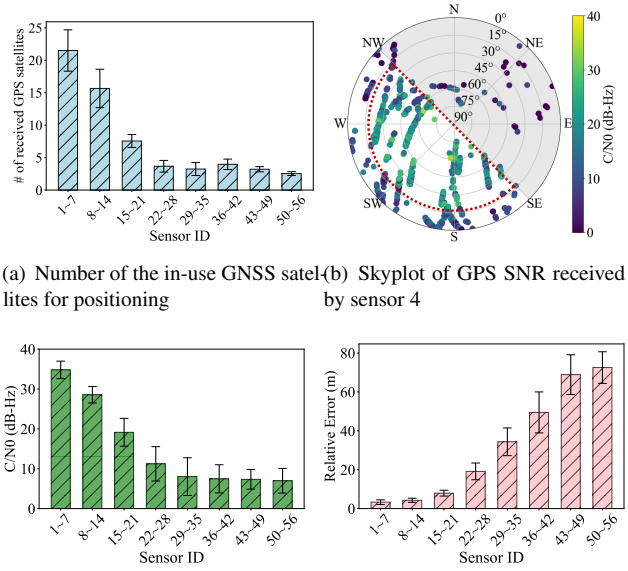

(a) Number of the in-use GNSS satellites for positioning (b) Skyplot of GPS SNR received by sensor 4

(c) SNR of received GNSS signals (d) Positioning error

Figure 3: Analysis of GNSS satellite signals received indoors over 24 hours with a southwest-facing window

across a large indoor space, which is more challenging. We observe that the elevation angles of users do not vary much while the azimurth angles vary a lot depending on the user location in the indoor space. Therefore, we strategically steer the satellite signals towards users in the elevation direction and scatter the signals to cover a wide azimuth angles for a broad coverage. We design a passive metasurface design that integrates steering and scattering capabilities using multiple metasurfaces and jointly optimizes their designs. (ii) We formulate an accurate indoor positioning algorithm that is not only compatible with passive metasurfaces but can also be seamlessly deployed on mobile devices. To the best of our knowledge, our work is the first work that uses a passive metasurface for enabling indoor GNSS positioning.

3 MEASUREMENT STUDY

While GNSS signals can theoretically penetrate indoors through windows, their signals are too weak to provide reliable indoor positioning services. In this section, we present a series of measurement studies to understand GNSS signal propagation and distribution indoors.

3.1 Indoor GNSS Signal Measurement

Figure 2 shows our GNSS indoor signal measurement setup. We use an array of GNSS chips to collect GNSS information instead of mobile phones because they can collect signal strength data for the entire indoor scene at once. This captures a comprehensive information about GNSS signals across space over an extended period of time. We select a spacious indoor area of 8×10m^2 with southwest-facing windows. GNSS

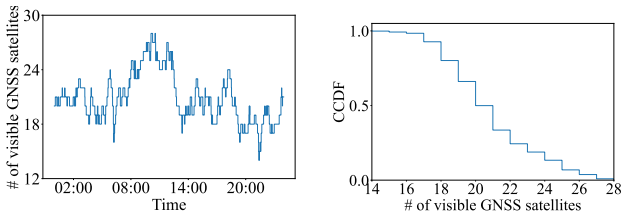

(a) Number of GNSS satellites visible above east-facing (az∈ [30°, 150°], el ∈ [0°, 90°])

(b) Complementary cumulative distribution function of visible GNSS satellites across all facing directions

Figure 4: Visibility analysis of GNSS satellites near the window of one building over 24 hours

sensors, arranged in a 7×8 configuration, are deployed at a height of around 1.4 m, which is the common height of a smartphone held by an adult. We use gt-u13 with a dual band GNSS antenna [4].

The basic principle of GNSS positioning systems is to use signals from at least *four* satellites for positioning [22]. Theoretically, if there are over four visible satellites with high SNR, the GNSS positioning can succeed. The accuracy and stability of positioning further improves with the number of visible satellites due to the increased number of constraints, which helps to restrict solution space [20]. Advanced techniques like Kalman filtering can also be used to combine signals from multiple satellites, reducing positioning errors [41]. Therefore, the two important indicators for GNSS positioning accuracy are the number of visible satellites and SNR or Carrier-to-Noise Density Ratio, denoted as C/N_0, which is the ratio of carrier power (C) to the noise density (N_0) of GNSS satellite signal. It can also be used to measure the strength and quality of the received GNSS signal.

We record GNSS raw data from these sensors for 24 hours, including message types, such as GPGSV, BDGSV, and GNRMC [6]. By examining these messages, we extract key GNSS positioning metrics, such as SNR and the number of visible satellites. Additionally, we record the latitude and longitude coordinates of the visible satellites to understand the geometric distribution of these satellites in space.

Upon collecting and analyzing data, we observe several interesting phenomena and draw the following conclusions:

- Satellite availability indoors is linked to proximity to windows. As shown in Figure 3(a), sensors closer to windows (1-7) receive signals from 21.5 GNSS satellites on average, while sensors farther away from the window (21-56) receive less than 5 satellites. This is because the satellite signals coming from a high elevation angle are directed downwards, making it difficult for them to penetrate deep into an indoor space.
- Figure 3(b) shows satellite skyplot trajectories measured by sensor 4 in 24 hours. Only GPS satellite trajectories are visualized for readability. We observe that signals with higher SNR come from the GPS satellites at higher elevation angles (shown in the red dotted line) near the window. If these signals coming from a high elevation angle could penetrate deeper indoors, they could improve indoor GNSS positioning due to their high SNR. Theoretically, the gray areas in Figure 3(b) are coverage blind spots for GNSS signals. However, in practice, some GNSS satellite signals can still be received in these areas due to the reflections from nearby buildings.
- Figure 3(a), (c), and (d) show a direct correlation between the SNR of satellite signals and positioning accuracy. Increasing SNR of reception signals and the number of visible GNSS satellites are crucial for accurate distance estimation and GNSS positioning.

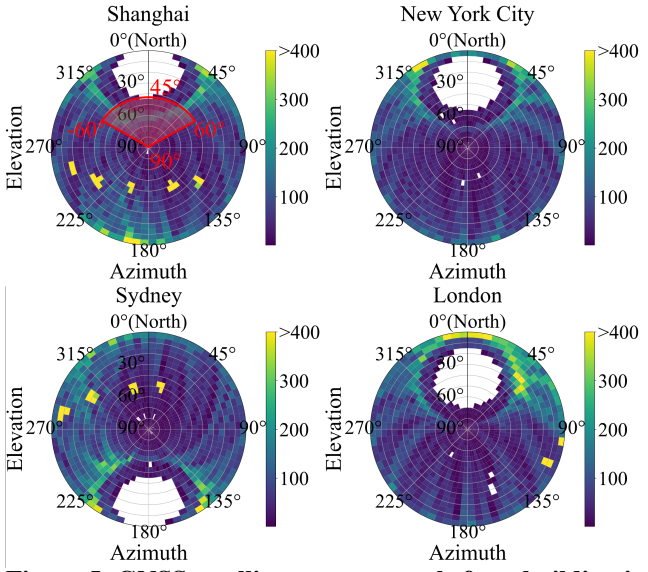

Figure 5: GNSS satellite coverage angle for a building in four different cities. The red sector in the top-left subfigure indicates coverage for north-facing windows, with azimuths from -60° to 60° and elevation from 45° to 90°

3.2 GNSS Coverage Analysis near Windows

To achieve accurate GNSS positioning indoors, it is essential to ensure a high SNR and high availability of GNSS signals. This can be achieved by effectively steering GNSS satellites' signals from higher elevation angles to propagate well inside. Additionally, for uniform distribution of GNSS signals across indoor areas, effective scattering is necessary to maximize coverage. However, this introduces an additional consideration: whether enough GNSS satellites are visible through the windows. To answer this question, we analyze the satellite signal coverage near windows using the GNSS system trajectory [7], geographic coordinates, and window direction. We select a building in a city facing east and calculate the coverage of GNSS satellites within the azimuth range of 30° to 150° and the elevation range of 0° to 90° over 24 hours.

The results are shown in Figure 4(a). We also analyze the situation of windows facing 36 different directions at 10° intervals and plot the complementary cumulative distribution function (CCDF) curve of the satellite coverage number, as shown in Figure 4(b). The analysis results indicate that at any location near a window, there is a 100% chance of seeing an average of at least 14 GNSS satellites in any direction during 24 hours, and a 50% chance of seeing up to 21 satellites. These numbers suggest that a sufficient number of satellites are visible for positioning at windows. If we can design a passive metasurface that effectively redirects GNSS signals from windows into indoor environments, we can potentially realize indoor GNSS positioning.

To optimize metasurface design using GNSS satellite trajectories, it is crucial to understand GNSS satellite incident angles across different orientations that windows face. Figure 5 illustrates the skyplot of GNSS satellite coverage for four major cities. The colorbar values represent the cumulative visibility time of all GNSS satellites at each angle over a 24-hour period. For a building situated in Shanghai with north-facing windows, to ensure that the metasurface covers satellite signals at all times, the elevation angle needs to be set between 45° and 90°. Since the azimuth angle is omnidirectional, we set the optimized azimuth angle to range from -60° to 60°, as shown by the red sector in Figure 5.

4 METASURFACE FOR INDOOR GNSS

We propose using passive metasurfaces to bring GNSS signals indoors to improve SNR and increase visible satellites, which can enable indoor GNSS positioning. However, two challenges arise: (1) designing a passive metasurface that can direct signals from satellites across various elevations and azimuths indoors while maintaining sufficient scattering capability is challenging due to the lack of programmability in passive metasurfaces, and (2) GNSS systems operate at two frequency bands from L1 and L5 bands, requiring our designed metasurface to effectively steer and scatter GNSS signals across both bands. We abstract the design into two parts: macro-design to determine the optimal phase map for effective steering and scattering, and micro-design to maintain high transmittance and nearly 360° phase control.

4.1 Macro-design: Optimizing Metasurface for Steering and Scattering

Our design aims to guide GNSS signals into indoor areas parallel to the ground through a passive metasurface (*i.e.*, in the elevation direction) and scatter them widely across the space (*i.e.*, in the azimurth direction) to achieve broad coverage. Unlike active metasurfaces, which have strong programmability to control EM waves in different ways, passive metasurfaces

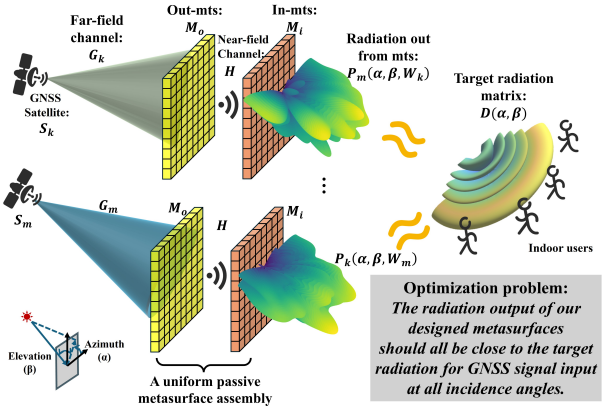

Figure 6: Modeling of steering and scattering metasurfaces and their associated optimization problem definition

have fixed phase modulation configuration files after fabrication, similar to lenses with specific functions. Therefore, designing a passive metasurface to manipulate EM waves with different incident angles to emit in the same steering and scattering ways seems impossible because light of a given frequency from one incident angle cannot propagate in different directions after passing through a single lens. And EM waves share the same property.

However, we observe that multiple lenses are powerful enough to allow light from different incident angles to converge at a single area. Therefore, our design uses a combination of multiple (*e.g.*, two) passive metasurfaces to let incident EM waves from different incident angles have similar outgoing trajectories. We create a channel model for GNSS EM wave propagation and formulate it as an optimization problem to jointly determine the phase profiles of outside and inside metasurfaces in the assembly system to create the desired beam patterns, as seen in Figure 6.

Channel from GNSS satellite to outside metasurface: We first develop a channel model from a GNSS satellite to the outside metasurface (out-mts in Figure 6). The structure of the out-mts is a 2D array consisting of $n \times n$ elements, equally spaced at a distance d. Let (i, j) denote the index of each element, where the element at the top left corner is $(0, 0)$ and serves as the reference element for the origin. Considering the far-field approximation for planar incoming wavefronts, we assume the GNSS signals arriving at each antenna element have the same amplitude. We then calculate the path difference ΔL to element (i, j) based on incident azimuth angle α_m and elevation angle β_m of the m-th GNSS satellite. The phase difference $\Delta\theta$ for element (i, j) can be derived as:

$$\Delta\theta_{m,(i,j)} = -\frac{2\pi f}{c}\left(id\sin(\beta_m)\cos(\alpha_m) + jd\sin(\beta_m)\sin(\alpha_m)\right) \quad (1)$$

Therefore, we define the channel matrix $\mathbf{G}$ to represent the EM wavefront of the GNSS signals arriving at the out-mts. Each element $G_{m,(i,j)}$ determines the complex channel response

from the m-th GNSS satellite to the (i, j)-th unit of the out-mts, where $G_{m,(i,j)} = A_{m,(i,j)} e^{\Delta\theta_{m,(i,j)}}$. Here, $A_{m,(i,j)}$ is the amplitude decay term, *i.e.*, 1.

Channel of outside metasurface: A metasurface element will change the incident EM waves through its own channel response: $M = Ae^{\theta}$, where A is the transmittance and θ is the phase shift. We denote the total channel matrix of the out-mts is **Mo**, where $\mathbf{Mo}_k = A_k e^{\theta_k}$ defines the channel response of the (i, j)-th cell, and the index value of k equals $i \cdot j$.

Channel between out-mts and in-mts: We define the channel matrix **H** between two sub-metasurfaces in the assembly system, where each element $H_{k,q}$ determines the complex channel response from the k-th, *i.e.*, (i_{out}, j_{out})-th, element in the out-mts to the q-th, *i.e.*, (i_{in}, j_{in})-th, element in the in-mts, where $H_{k,q} = A_{k,q} e^{\theta_{k,q}}$, $A_{k,q}$ is the decay term, and $\theta_{k,q}$ is the phase delay term. For $A_{k,q}$, we derive $A_{k,q} = \frac{d}{\sqrt{2\pi d_{k,q}^2}} \cdot \sqrt{cos\phi_{k,q}}$ according to the free-space path loss [35], where $d_{k,q}$ is the distance between the k-th out-mts element and q-th in-mts element, and d is the element spacings of metasurface, the same spacing between the out-mts and in-mts. $\phi_{k,q}$ is the incident angle from out-mts to in-mts. We calculate the phase delay term as $\theta_{k,q} = -\frac{2\pi d_{k,q}}{\lambda}$.

Channel of inside metasurface: The total channel matrix of in-mts is **Mi**, where $\mathbf{Mi}_q$ defines the channel response of the q-th cell in in-mts.

Radiation from in-mts: We aim to design a metasurface to enable steering GNSS signals deep into an indoor space in the elevation direction and scattering them to cover a wide azimurth direction. We model the EM field radiated from the inside metasurface as follow. For a $n \times n$ array in-mts, we derive the Array Factor, *i.e.*, AF(α, β), to calculate the directional map, which is a superposition of the radiation patterns of all the array elements using the following formula:

$$AF(\alpha, \beta) = \sum_{i=0}^{N-1} \sum_{j=0}^{N-1} w_{i,j} \cdot e^{-j\frac{2\pi}{\lambda}(id \sin\beta\cos\alpha + jd \sin\beta \sin\alpha)} \quad (2)$$

α and β are the radiation angles from the in-mts in the azimuth and elevation directions, respectively. The detailed definitions of α and β are shown in Figure 6. $w_{i,j}$ is the radiation complex weight of the $(i, j)-$th element in the in-mts. The direction map $P(\alpha, \beta)$ can be obtained by normalization $AF(\alpha, \beta)$:

$$P(\alpha, \beta) = \frac{||AF(\alpha, \beta)||}{\max(||AF(\alpha, \beta)||)} \quad (3)$$

Final optimization problem: Our goal is for the metasurfaces to distribute the EM waves across an azimuth direction from α_1 to α_2 (*e.g.*, from -60° to 60°) and an elevation range from β_1 to β_2 (*e.g.*, from -5° to 5° given the typical height of a smartphone carried by a user). Therefore, our objective is to make the directional map radiated from the in-mts to approach the desired directional map, $D(\alpha, \beta)$, which should have a relatively uniform gain over the desired range and decay rapidly to 0 or close to 0 outside this range. The desired directional map is defined as follows:

$$D(\alpha, \beta) = \begin{cases} 1, & \text{if } \alpha \in [\alpha_1, \alpha_2] \text{ and } \beta \in [\beta_1, \beta_2] \\ 0, & \text{others} \end{cases} \quad (4)$$

For the $m-$th GNSS satellite in the view of the window, we can obtain the total channel response $\mathbf{W_k}$ of the in-mts as: $\mathbf{G_m MoHMi}$. Therefore we can obtain each channel response of the $(i, j)-$th element in in-mts, and use Equation 2 we can obtain the steering and scattering ability of the metasurface for the incoming $m-$th GNSS signals. The final optimization problem is as follow:

$$\min_{Mi,Mo} \sum_{m=1}^{K} \int \int \left(P(\alpha, \beta, W_k) - D(\alpha, \beta)\right)^2 d\alpha d\beta \quad (5)$$

In the above optimization problem, we discretize the continuous azimuth and elevation angular space into a grid with a precision of (1°, 1°), and then we perform a summation over each grid point as a substitute for the integration over the entire angular space.

To summarize, optimizing GNSS metasurfaces involves the following three steps: (i) we estimate the azimuth and elevation angles of visible satellites from the target window using their orientation and coordinates inside a GNSS simulator; (ii) we define the range of angles required for steering and scattering signals into the indoor space; (iii) we utilize gradient descent and the Adam optimizer, directed by our optimization equation Equation 5, to determine the optimal phase maps for the outer and inner metasurfaces, denoted as **Mo** and **Mi**, respectively, to best approximate the desired phase map.

4.2 Micro-design: Meta-atom Design for GNSS Scenarios

Our metasurface is designed for accurate steering and scattering GNSS signals. The design of its meta-atoms must fulfill the transmission requirements for GNSS satellite scenarios, characterized by: (1) multi-band frequencies support; (2) wide incident angle adaptability; (3) high transmission efficiency; and (4) nearly 360° phase control capability. Drawing inspiration from the meta-atom designs for LEO satellite communication [34], we adapt these concepts in our GNSS metasurface application. The detailed meta-atom model is shown in Figure 7(a). The central cross is designed to resonate at around 1.56-1.65 GHz, where varying the L_1 parameter facilitates different phase delays within that band. Similarly, the peripheral crosses resonate at around 1.17-1.28 GHz, with the L_2 parameter being adjustable to modulate phase delays at that band.

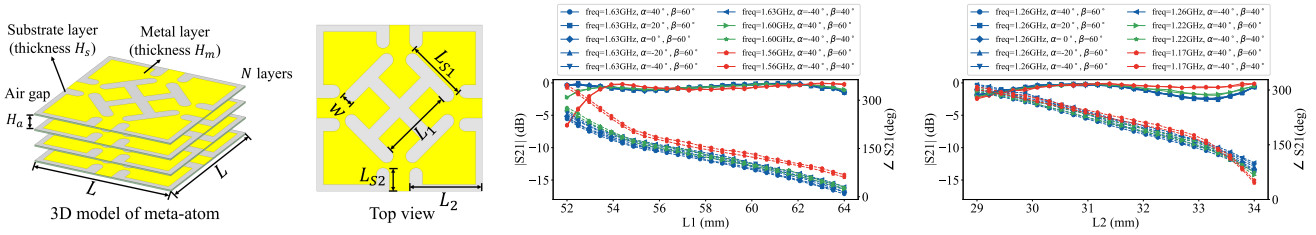

(a) Meta-atom structure model (b) L1 band performance, with L_2 = 30 mm (c) L5 band performance, with L_1 = 60 mm

Figure 7: Meta-atom structure (a) for both out-mts and in-mts and the transmission amplitude (|S21|, solid lines in (b) and (c)) and phase responses (∠ S21, dashed lines in (b) and (c)) of the optimized meta-atom with parameters in Table 2 at GNSS dual bands across various incident angles

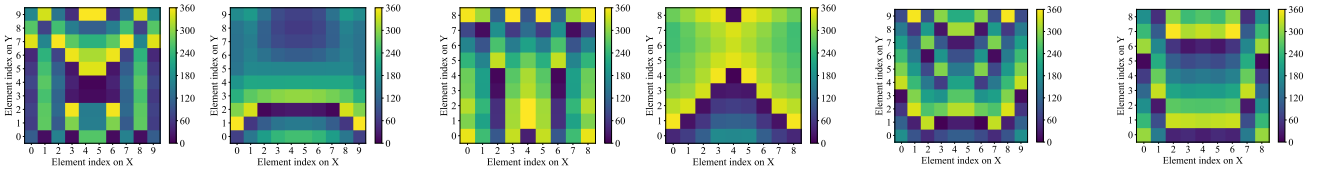

(a) 10×10 phase map at L1 band, left is the out-mts, right is the in-mts (b) 9×9 phase map at L5 band, left is the out-mts, right is the in-mts (c) 10×10 phase map at L1 band (d) 9×9 phase map at L1 band

Figure 8: Optimized phase maps for outside and inside metasurfaces at L1 and L5 bands. (a)-(b) are for the 2-layer metasurface assembly, and (c)-(d) are for the 1-layer metasurface

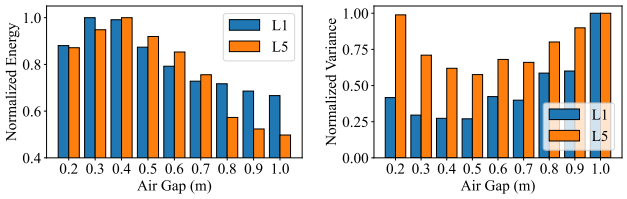

(a) Energy metric (b) Variance metric

Figure 9: Determining the optimal air gap between the out-mts and in-mts for the improved steering and scattering performance. Our findings indicate that an air gap of 0.4 meters provides the best performance

This innovative method allows for effective phase control at two distinct frequency bands.

We apply the same meta-atom optimization method in [34] to ensure that the designed meta-atoms fulfill the operational demands of GNSS scenarios. Table 2 shows these hyperparameters. The simulation performance of the optimized meta-atoms using the HFSS simulator [10] is shown in Figure 7(b) and (c). We find that the optimized design could maintain high transmittance in both the L1 and L5 bands (within -1 dB attenuation) while supporting around 250° phase control capability in both bands. It is important to note that the dual-band meta-atoms are achieved through staggered cross-like structures, resulting in a difference in the total number of outer crosses compared to the inner ones. For instance, if we fabricate an 10×10 metasurface, the number of meta-atoms responsible for the L5 band will be 10×10, whereas the number for the L1 band will be 9×9. Thus, we optimize the phase maps for both frequency bands separately. Finally, based on the optimized phase maps and the relationship of the geometric parameters L_1 and L_2 corresponding to the phase delays as shown in Figure 7(b) and (c), we can obtain the metasurfaces' geometric pattern array for the final manufacturing stage.

Para.	N	H_s	H_m	w	L	H_a	L_{S1}	L_{S2}
Value	4	$1mm$	$0.1um$	$8mm$	$10cm$	$10mm$	$L_1/2$	$10mm$

Table 2: Final structure of unit cell design, substrate layer is PVC and A4 paper, metal layer is Aluminum foil

4.3 Simulation-based Performance Analysis of Optimized Metasurfaces

Through macroscopic and microscopic design strategies, we derive an optimized metasurface design capable of efficiently guiding GNSS signals into the indoor space. For this optimized metasurface, we set the range of azimuth angles for satellite signals incident on the outside metasurface to be between -75° and 75°, with an elevation angle ranges from 15° to 80°. The radiation range of the inside metasurface is optimized to achieve the azimuth angles ranging from -60° to 60° and elevation angles from -5° to 5°. This setup allows the EM waves to span 1.2 to 1.8 m in height, suitable for a $>$ 10 m deep indoor area when the metasurface is placed at a height of 1.6 m.

The design of the metasurface assembly is greatly influenced by the air gap between the out-mts and in-mts, affecting the overall wavefront control performance. An too small air gap causes the two metasurfaces to act as one, whereas a

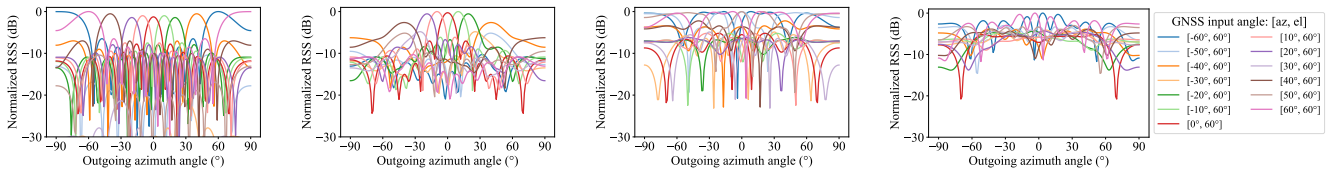

(a) 1-layer mts w/o optimization (b) 2-layer mts w/o optimization (c) 1-layer mts w/ optimization (d) 2-layer mts w/ optimization

Figure 10: 1D beam pattern radiated from metasurfaces across various GNSS incident angles at L1 band, these subfigures share the same legends

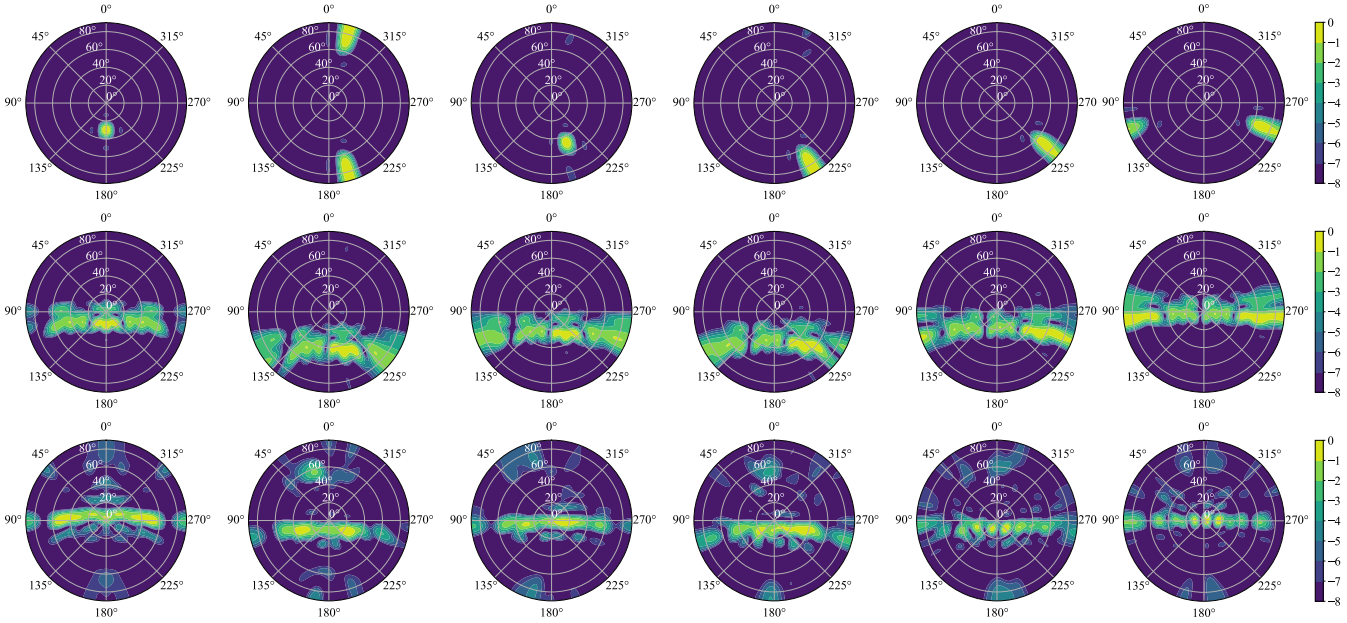

(a) az=0°, el=30° (b) az=0.0°, el=75° (c) az=15°, el=45° (d) az=30°, el=75° (e) az=45°, el=60° (f) az=60°, el=45°

Figure 11: Radiation beam pattern emitted from the metasurfaces (10×10) across GNSS incident angles at L5 band, and the first row represents unoptimized 2-layer metasurface, the second row depicts the optimized 1-layer metasurface, while the third row depicts the optimized 2-layer metasurface (*i.e.*, out-mts and in-mts). The results demonstrate that the optimized metasurfaces are capable of effectively steering and scattering GNSS signals across different incident angles

too large gap diminishes their collaborative effect. Hence, identifying the optimal air gap is essential. We evaluate the assembly's performance using two metrics: (i) the energy preserved during transmission by the metasurface, and (ii) variance, which reflects the metasurface's ability to maintain stable performance across different GNSS incident signal angles and outgoing scattering angles. The simulation results are shown in Figure 9, and we choose 0.4 m as the optimal air gap, aligning with a typical outer wall thicknesses of 0.25~0.4 m.

We optimize the phase map configurations for both the outside and inside metasurfaces for the L1 and L5 frequency bands, with optimization results for the two-layer metasurfaces as shown in Figure 8(a)-(b). We also use a similar model to solve for the optimal phase configuration for the case of a metasurface with only 1 layer, as shown in Figure 8(c)-(d).

Subsequently, we verify the effectiveness of the optimized 2-layer metasurface by selecting phase maps of size 10×10 for validation in the L1 band and phase maps of size 9×9 for validation in the L5 band. The 1D radiation pattern of the indoor metasurface at L1 band is shown in Figure 10. First, from Figure 10(a) and (b), we observe that without optimization each element in the 1-layer and 2-layer metasurfaces has the same phase delay, which causes the indoor beam pattern of the GNSS signals varies significantly with different incident angles, lacking a scattering effect and failing to cover all indoor areas. With optimization, they are found to be capable of steering and scattering the incident GNSS signal. To facilitate comparison of the metasurface performance, we also plot the corresponding 2D radiation beam pattern, as shown in Figure 11. The optimized 1-layer metasurface has limited wavefront control capability. When GNSS signals come from various angles, the outgoing radiation pattern is deflected as the incidence angle changes. Although it can perform a certain degree of scattering across incident angles, it cannot

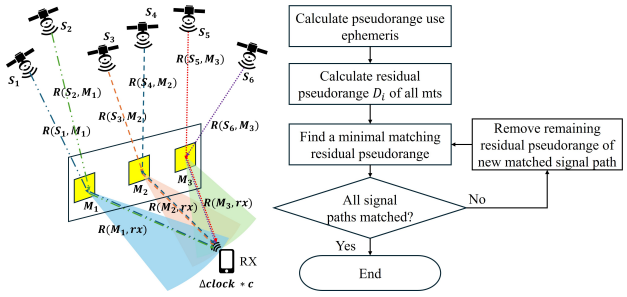

(a) Core idea (b) Metasurface matching algo.

Figure 12: Metasurface-compatible positioning algorithm

consistently steer the GNSS signals. We also observe that our optimized 2-layer metasurfaces not only effectively scatters the GNSS signals across azimuth angles (*e.g.*, offering ~180° azimurth coverage) but also performs effective steering at elevation angles (*e.g.*, covering 10° elevation angles), bringing signals close to the horizontal direction to reach farther inside.

5 LOCALIZATION ALGORITHM

As metasurfaces enable GNSS signals to penetrate indoors, the signal path from satellites to users now includes an additional node, which makes conventional GNSS localization algorithms inappropriate. In this section, we introduce a novel positioning algorithm that leverages GNSS messages to achieve accurate indoor localization. Our proposed algorithm can be directly deployable on mobile phones, as GNSS messages can be accessed directly through Android APIs [8].

5.1 Localizing using Known Metasurfaces

Figure 12(a) shows the schematic of our positioning algorithm. We first explain the core idea of our positioning algorithm assuming that we know which metasurface each GNSS signal passes through to reach the user. Let $PR(S_i, M_j, rx)$ represent the pseudorange of the ith satellite signal that passes through the jth metasurface to reach the receiver. We have $PR(S_i, M_j, rx) = R(S_i, M_j) + R(M_j, rx) + \Delta clock * c$, where $R(S_i, M_j)$ is the distance between the ith satellite and the jth metasurface, $R(M_j, rx)$ is the distance between the jth metasurface and the receiver, $\Delta clock$ is the clock bias between the satellite and the receiver, and c is the speed of light. Therefore, the GNSS receiver can determine its position as follows: (i) Compute the distance between the user and metasurface that the GNSS signal passes through as $R(M_j, rx) + clock = PR(S_i, M_j, rx) - R(S_i, M_j) = RC_{ij}$, where $PR(S_i, M_j, rx)$ is measured by the GNSS receiver, $R(S_i, M_j)$ can be calculated based on the GNSS ephemeris and the known position of the metasurface itself, and $\Delta clock$ is a fixed value for a given user. We use RC_{ij} to represent the distance and clock bias between the j-th metasurface and the user. (ii) Use trilateration to compute the user's coordinates. The trilateration step is the same as the standard GNSS trilateration positioning, except that we use the metasurfaces as anchor points, which can be treated as virtual satellites.

To determine the unknown three-dimensional coordinates and unknown clock bias from the satellites, GNSS requires four satellites to obtain line-of-sight measurements to estimate four unknowns. Similarly, in our case, the GNSS receiver needs to receive signals from at least four metasurfaces for positioning. In indoor positioning, the Z-axis information can generally be obtained from the barometeric pressure or other external information (*e.g.*, when the user knows the floor they are on and the height of their phone above the ground, we only need to receive signals from three metasurfaces to obtain the user's position).

5.2 Matching Paths with Metasurfaces

Our localization algorithm requires identification of the specific metasurface each GNSS signal passes through indoors. Thus, we need an algorithm that can automatically determine the metasurface that a signal traverses through. One idea is to embed a unique signature in the signal altered by each metasurface for easy identification. Yet, this is impractical with the passive metasurfaces. To address this need, we develop a novel matching algorithm. As shown in Figure 12(a), we observe that signals from different satellites going through the same metasurface share the same path from the metasurface to the GNSS receiver (*i.e.*, $PR(S_1, M_j, rx) - R(S_1, M_j) \approx PR(S_2, M_j, rx) - R(S_2, M_j) \approx ... \approx PR(S_i, M_j, rx) - R(S_i, M_j)$, when satellites 1, 2, ... i go through the j-th metasurface). Thus, we can use this observation to determine the metasurface through which the signal passes.

The GNSS receiver first cycles through all Pseudorandom Noise (PRN) codes used within its range, which represent unique GNSS satellites, and we can determine the accurate coordinates of the satellites from ephemeris data. For each received GNSS signal, we can obtain the corresponding pseudorange $PR(S_i, rx)$ between the i-th satellite and receiver rx. The GNSS receiver (whether a GNSS chip or a GNSS module in a phone) only receives the unique path information from the current satellite, as its phase-locked loop only locks onto the signal with the highest received energy [2]. Next, we enumerate each possible reflecting surface j and calculate the distance between reflecting surface j and receiver rx to determine which one is reliable. Specifically, we have:

$$D_i = PR(S_i, rx) - \begin{bmatrix} R(S_i, M_1) \\ R(S_i, M_2) \\ \vdots \\ R(S_i, M_j) \end{bmatrix} = \begin{bmatrix} D(S_i, M_1, rx) \\ D(S_i, M_2, rx) \\ \vdots \\ D(S_i, M_j, rx) \end{bmatrix} \quad (6)$$

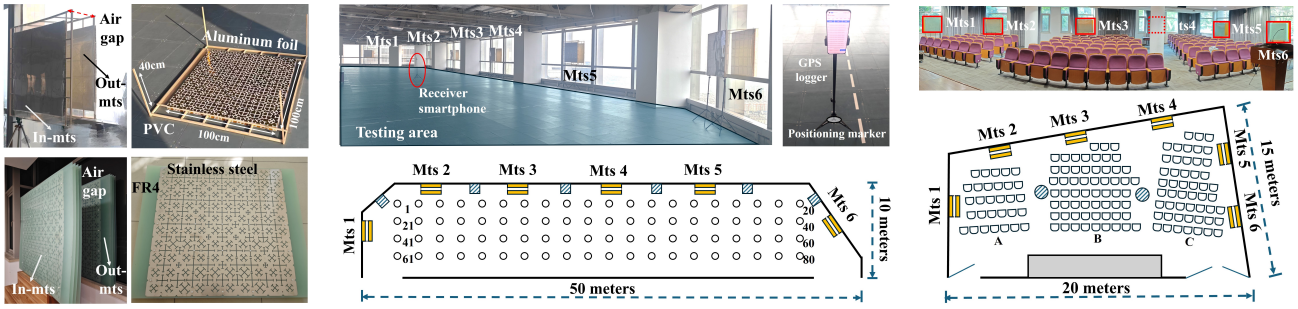

(a) Two types of fabricated GPMS (b) Indoor test scenario 1: office floor (c) Indoor test scenario 2: lecture room

Figure 13: Experimental setup for measuring indoor GNSS satellite signal quality and indoor positioning accuracy with deployment of our proposed metasurfaces

where $D(S_i, M_j, rx)$ represents the remaining pseudorange if the satellite signal goes through metasurface j.

To determine the reflecting surface that each path traverses, we develop a greedy heuristic algorithm. The detailed algorithm pipeline is shown in Figure 12(b). Each time, we compare each combination of $D_{s_{i_1}}$ and $D_{s_{i_2}}$ to find the best matching residual pseudorange. Then, we remove any pseudoranges that still pass through these two satellites, as each satellite signal should only pass through one reflecting surface. We repeat this process until all signals match with a reflecting surface. Our algorithm can be applied to distance estimation based on either pseudorange or carrier phase. Additionally, we can use multiple signals from satellites that pass through the same reflecting surface to estimate the distance between the reflecting surface and the receiver to improve accuracy.

6 EVALUATION

6.1 Experimental Setup

Metasurface fabrication: We utilize two methods to fabricate large-scale metasurfaces for GNSS: (i) a highly economical process based on hot stamping technology [27], and (ii) metal cutting, which offers better performance. The first method uses A4 paper, plastic sheets (~1 mm thick), aluminum foil hot stamping film, and wooden strips. First, we use a laser printer to create the desired pattern on the paper. Next, we place the aluminum foil hot stamping film over the printed pattern and pass through a laminator. This step makes the metallic powder in the foil bond with the toner. After peeling off the aluminum foil, the metallic pattern remains on the paper. Finally we use wooden strips to create the required air gaps between the inner and outer metasurfaces. The second method involves cutting metal plates, like stainless steel plate (with a thickness of around 0.5 mm), and attaching the cut metal plates to an FR4 substrate. Nylon posts are then used to secure the air gap between each layer. We also incorporate materials, such as stainless steel and FR4, into meta-atom HFSS simulations and determine the structure parameters to achieve ultra-high transmittance (>95%) and maximum phase modulation capability (~300°). Table 3 shows the optimized meta-atom hyperparameters. We use the optimized phase maps shown in Figure 8 for fabrications. Figure 13(a) shows our prototype.

Para.	N	H_s	H_m	w	L	H_a	L_{S1}	L_{S2}
Value	4	$1mm$	$0.5mm$	$5mm$	$10cm$	$25mm$	$L_1/3$	$6mm$

Table 3: Final structure of unit cell design, substrate layer is FR4, metal layer is stainless steel

GNSS coverage measurement and indoor positioning experiment setup: We verify the positioning accuracy of our system at two indoor spaces: one-floor in an office building spanning ~10×50 m^2 and a lecture room spanning ~20×15 m^2. To cover the entire space, we deploy six metasurfaces at both places, as shown in Figure 13(b) and (c). We employ the same experimental setup as described in section 3 to evaluate the performance of our metasurface. To ensure fairness, we deploy the designed metasurface on a window at the same indoor space and record data from the GNSS sensor array over 24 hours. To quantify the localization error, we select 80 points inside the office floor, using floor tiles as markers to calculate their exact geographical coordinates as the ground truth.

GNSS-based indoor positioning on Android phones: We implement an indoor GNSS positioning app on Android smartphones. Specifically, we use GNSS APIs [8] to obtain the real-time raw data, extract the pseudorange information and ToF from each GNSS satellite, and then calculate the user's indoor position using the algorithm presented in section 5. We use a Xiaomi 11 Pro smartphone equipped with our indoor positioning app. We support the smartphone on a tripod at each marker and record the estimated positions.

6.2 Performance Results

6.2.1 Indoor GNSS signal coverage. To assess the GNSS indoor coverage enhancement, our metasurfaces support L1

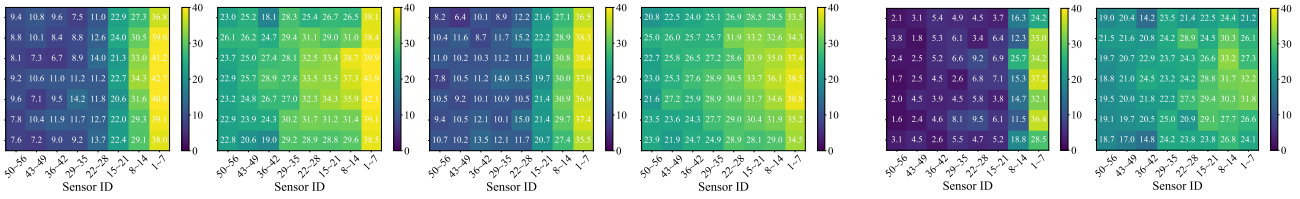

(a) L1 band w/o mts (b) L1 band w/ mts (c) L5 band w/o mts (d) L5 band w/ mts

Figure 14: Comparison of the measured C/N0 of received GNSS signals indoors across two GNSS frequency bands

(a) w/o mts (b) w/ mts

Figure 15: Comparison of the number of visible in-use GNSS satellites

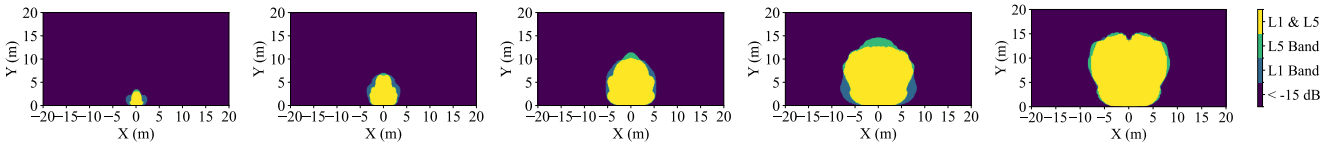

(a) 30cm×30cm (b) 50cm×50cm (c) 70cm×70cm (d) 90cm×90cm (e) 100cm×100cm

Figure 16: Comparison of metasurface size and simulated coverage capability. Both the out-mts and in-mts share the same size, and the coverage for each size is the result optimized by our algorithm in subsection 4.1

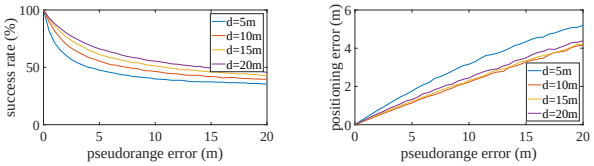

(a) Matching mts success rate (b) Positioning error

Figure 17: Simulation results of metasurface matching success rates and positioning errors under various pseudorange errors and spacings between two matesurfaces

and L5 bands. We place 7×8 GNSS chips, as shown in Figure 2(a) to evaluate performance. Initially, we set the chips to receive only L1 band signals, collecting data for 24 hours with and without the metasurfaces. We repeat this process for the L5 band. We analyze the SNR data from all GNSS satellites captured by the 56 sensors, and show the average SNR in Figure 14. The experimental results indicate that our metasurface can effectively steer and scatter outdoor GNSS signals. It increases C/N0 by 14.8 dB-Hz of in the L1 band and by 13.2 dB-Hz in the L5 band for positions that are located farthest from windows. This also confirms the multi-frequency bands support of our designed metasurface. We visualize the number of visible GNSS satellites at each sensor, as shown in Figure 15. We find that improving the SNR increases the number of visible GNSS satellites from 3.6 to 21.5 on average for positions that are located farthest from windows.

Metasurface size vs. coverage performance: Initially, we define indoor GNSS coverage. An area is considered to have effective coverage if the indoor signal attenuation, relative to the GNSS signal energy at the window, does not exceed -15 dB. Furthermore, this effective coverage must be achieved simultaneously across both the L1 and L5 frequency bands. The coverage distance is defined as the average of the effective coverage range within the ±60° radiation range of the metasurface. Due to energy conservation, the metasurface' aperture dictates the coverage performance by scattering signals. We use simulation to compare indoor GNSS coverage performance under different metasurface sizes. Figure 16 summarizes the results. We use 10 cm as the unit length of the meta-atom. To maintain an azimuth range of [-60°, 60°], a metasurface of size 0.5×0.5 m^2 achieves a maximum coverage distance of 4.93 m, while a 1×1 m^2 metasurface can reach up to 12.56 m. Therefore, we recommend using larger metasurfaces for increased coverage distance.

6.2.2 Indoor GNSS positioning. We evaluate the performance of our indoor GNSS positioning algorithm, which comprises two components: matching metasurface algorithm and indoor positioning algorithm. First, to evaluate the matching performance of our algorithm, we develop a simulator to test how effectively it performs under a range of GNSS pseudorange errors and varying spacing between metasurfaces. We assume that each GNSS metasurface has a coverage range of 20 m. Figure 17 summarizes the results, where d represents the spacing between metasurfaces. It is evident from the figure that the matching success rate decreases as the pseudorange errors increase. Nevertheless, the rate of this decline is less pronounced when the spacing between metasurfaces is larger.

Data collection of the indoor positioning experiments are conducted using the setups shown in Figure 13(b) and (c). At the office floor, we mark the user's test points with markers, and use their absolute latitude and longitude coordinates as the ground truth to compare positioning accuracy. In the lecture room, we use chairs to mark the test points and divide the

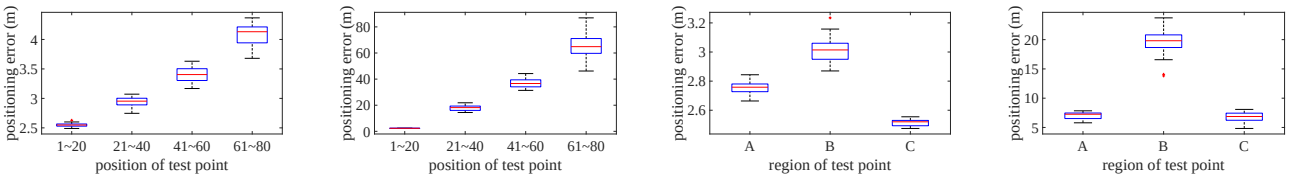

(a) Office floor: w/ mts (b) Office floor: w/o mts (c) Lecture room: w/ mts (d) Lecture room: w/o mts

Figure 18: Indoor GNSS positioning error w/ and w/o our proposed GPMS in two testing indoor environments

space into three areas: A, B, and C, with A and C being closer to the windows. In the office floor, the indoor positioning errors with our proposed GPMS are reported in Figure 18(a). Our measurements show that the average position errors for each row of test points are 2.6 m, 3.0 m, 3.4 m, and 4.1 m, respectively. When considering the collective data from all test points, the average positioning error is 3.2 m. In comparison, positioning errors in scenarios without metasurfaces, as shown in Figure 18(b), leads to increased positioning errors with larger receiver distance from the window due to the sharp decrease in SNR. The average positioning error near the window is about 2.3 m, but degrades to 17.8 m, 38.1 m, and 64.2 m as we get farther away. These results demonstrate the effectiveness of our system. In the lecture room, our GPMS indoor positioning system is utilized, resulting in average location errors of 2.7 m, 3.0 m, and 2.5 m in the regions A, B, and C, respectively. In comparison, the corresponding errors without metasurfaces are 7.25 m, 19.3 m, and 6.82 m, respectively, which indicates our approach yields significant improvement in indoor localization. The aforementioned experimental results demonstrate that our GPMS system significantly enhances positioning accuracy in two different indoor settings. This also indicates that our optimized two-layer metasurface assembly can improve the indoor GNSS's SNR through steering and scattering, which in turn improves indoor GNSS positioning accuracy.

7 DISCUSSION

Deployment cost: We provide a comprehensive breakdown of the hardware manufacturing and assembly costs for a complete metasurface assembly, which includes both the outside and inside metasurfaces. All of the following cost analyses are based on a 1 m^2 metasurface. Using the hot stamping fabrication method, the cost of aluminum foil is \$3, A4 paper is \$0.5, PVC is \$6, and the cost of wooden frames used to fix the air gap is \$4. The total cost for one metasurface assembly is \$13.5, and it weighs approximately 6.5 kg. Alternatively, using the metal cutting fabrication method, the cost of metal cutting (including the stainless steel materials) is \$120, the cost of FR4 substrate is \$40, and the cost of nylon columns used to fix the air gap is \$6. The total cost for one metasurface assembly is \$166, and it weighs approximately 11 kg. Each metasurface assembly will be accompanied by 2-4 tripods, which cost approximately \$5 each. Mass production can significantly reduce the cost of both fabrication methods.

Through-wall metasurface design: In indoor GNSS positioning systems, there is a need to solve the problem of signal penetration through walls. Metasurfaces can be deployed to help GNSS signals penetrate the walls. This can be achieved by designing the metasurface to match the impedance of the wall, which increases the efficiency of EM wave penetration [33]. In our proposed metasurface, impedance matching can be added to create a wall-penetrating friendly solution. We leave this as future work.

Materials for metasurface fabrication: Our proposed metasurface design for indoor GNSS positioning is versatile in terms of fabrication materials. In this paper, we have demonstrated the feasibility of our design using two different fabrication methods. Additionally, transparent conductive materials, such as Indium-Tin-Oxide (ITO) [48] can be utilized to manufacture the metasurface, enabling its deployment on windows without obstructing light. The feasibility of fabricating metasurfaces with transparent conductive materials has also been corroborated by certain transparent metasurface cases in the industry [1, 5].

8 CONCLUSION

In this paper, we propose GPMS, a system that enables indoor GNSS positioning using passive metasurface techniques. Our passive metasurfaces can effectively redirect outdoor GNSS signals indoors to enhance SNR and increase the number of visible satellites. Our optimized metasurfaces can be fabricated using transparent conductive materials and integrated seamlessly with windows. We also develop an indoor localization algorithm to support the use of passive metasurfaces. Our evaluation results show it is promising to use passive metasurfaces to enable GNSS indoor positioning.

ACKNOWLEDGMENTS

We thank the anonymous reviewers for their constructive comments. This work is supported in part by NSFC (No. 61936015, 62072306, 62341201, 62122095, 62432004 and 62072472) and by a grant from the Guoqiang Institute, Tsinghua University.

REFERENCES

[1] Docomo uses 5g to test new transparent dynamic metasurface. https://futureiot.tech/docomo-uses-5g-to-test-new-transparent-dynamic-metasurface/.

[2] Fundamentals of phase locked loops (plls). https://www.analog.com/media/en/training-seminars/tutorials/MT-086.pdf.

[3] Gps repeaters. https://www.navtechgps.com/departments/rf-networking-das/repeaters/.

[4] Gt-u13 dual-frequency gnss flight control satellite positioning and navigation module g ps beidou glonass irnss system. https://www.amazon.com/CRUMPS-Dual-Frequency-Satellite-Positioning-Navigation/dp/B0CF2V34YH.

[5] Kyocera develops transmissive metasurface technology. https://www.designing-electronics.com/kyocera-develops-transmissive-metasurface-technology/.

[6] Nmea-0183 messages: Overview. https://receiverhelp.trimble.com/alloy-gnss/en-us/NMEA-0183messages_MessageOverview.html.

[7] Norad gp element sets current data. https://celestrak.org/NORAD/elements/.

[8] Raw gnss measurements. https://developer.android.com/develop/sensors-and-location/sensors/gnss.

[9] S. Aggarwal, R. K. Sheshadri, K. Sundaresan, and D. Koutsonikolas. Is wifi 802.11 mc fine time measurement ready for prime-time localization? In *Proceedings of the 16th ACM Workshop on Wireless Network Testbeds, Experimental evaluation & CHaracterization*, pages 1–8, 2022.

[10] Ansys. Ansys hfss best-in-class 3d high frequency electromagnetic simulation software. https://www.ansys.com/products/electronics/ansys-hfss.

[11] R. Ayyalasomayajula, D. Vasisht, and D. Bharadia. Bloc: Csi-based accurate localization for ble tags. In *Proceedings of the 14th International Conference on emerging Networking EXperiments and Technologies*, pages 126–138, 2018.

[12] S. Bhamidipati and G. X. Gao. Gps multireceiver joint direct time estimation and spoofer localization. *IEEE Transactions on Aerospace and Electronic Systems*, 55(4):1907–1919, 2018.

[13] G. S. de Blasio, A. Quesada-Arencibia, C. R. García, and J. C. Rodríguez-Rodríguez. Bluetooth low energy technology applied to indoor positioning systems: An overview. In *Computer Aided Systems Theory–EUROCAST 2019: 17th International Conference, Las Palmas de Gran Canaria, Spain, February 17–22, 2019, Revised Selected Papers, Part I 17*, pages 83–90. Springer, 2020.

[14] H. Deilamsalehy and T. C. Havens. Sensor fused three-dimensional localization using imu, camera and lidar. In *2016 IEEE SENSORS*, pages 1–3. IEEE, 2016.

[15] H. Dong, Y. Xie, X. Zhang, W. Wang, X. Zhang, and J. He. Gpsmirror: Expanding accurate gps positioning to shadowed and indoor regions with backscatter. *arXiv preprint arXiv:2304.07572*, 2023.

[16] P. S. Farahsari, A. Farahzadi, J. Rezazadeh, and A. Bagheri. A survey on indoor positioning systems for iot-based applications. *IEEE Internet of Things Journal*, 9(10):7680–7699, 2022.

[17] S. He and S.-H. G. Chan. Wi-fi fingerprint-based indoor positioning: Recent advances and comparisons. *IEEE Communications Surveys & Tutorials*, 18(1):466–490, 2015.

[18] S. He and K. G. Shin. Geomagnetism for smartphone-based indoor localization: Challenges, advances, and comparisons. *ACM Computing Surveys (CSUR)*, 50(6):1–37, 2017.

[19] Y. Hu, F. Qian, Z. Yin, Z. Li, Z. Ji, Y. Han, Q. Xu, and W. Jiang. Experience: Practical indoor localization for malls. In *Proceedings of the 28th Annual International Conference on Mobile Computing and Networking*, pages 82–93, 2022.

[20] J. Huang, R. Yang, W. Gao, and X. Zhan. Geometric characterization on gnss direct position estimation in navigation domain. *IEEE Transactions on Aerospace and Electronic Systems*, 2024.

[21] A. R. Jimenez, F. Seco, C. Prieto, and J. Guevara. A comparison of pedestrian dead-reckoning algorithms using a low-cost mems imu. In *2009 IEEE International Symposium on Intelligent Signal Processing*, pages 37–42. IEEE, 2009.

[22] E. D. Kaplan and C. Hegarty. *Understanding GPS/GNSS: principles and applications*. Artech house, 2017.

[23] H. Kuusniemi and G. Lachapelle. Gnss signal reliability testing in urban and indoor environments. In *Proceedings of the 2004 national technical meeting of the institute of navigation*, pages 210–224, 2004.

[24] B. Liang, P. Wang, R. Zhao, H. Guo, P. Zhang, J. Guo, S. Zhu, H. H. Liu, X. Zhang, and C. Xu. {RF-Chord}: Towards deployable {RFID} localization system for logistic networks. In *20th USENIX Symposium on Networked Systems Design and Implementation (NSDI 23)*, pages 1783–1799, 2023.

[25] C. X. Lu, Y. Li, P. Zhao, C. Chen, L. Xie, H. Wen, R. Tan, and N. Trigoni. Simultaneous localization and mapping with power network electromagnetic field. In *Proceedings of the 24th annual international conference on mobile computing and networking*, pages 607–622, 2018.

[26] Z. Luo, Q. Zhang, Y. Ma, M. Singh, and F. Adib. 3d backscatter localization for {Fine-Grained} robotics. In *16th USENIX Symposium on Networked Systems Design and Implementation (NSDI 19)*, pages 765–782, 2019.

[27] R. Ma, S. Zheng, H. Pan, L. Qiu, X. Chen, L. Liu, Y. Liu, W. Hu, and J. Ren. Automs: Automated service for mmwave coverage optimization using low-cost metasurfaces. In *Proceedings of the 30th Annual International Conference on Mobile Computing and Networking*, pages 62–76, 2024.

[28] Y. Ma, N. Selby, and F. Adib. Minding the billions: Ultra-wideband localization for deployed rfid tags. In *Proceedings of the 23rd annual international conference on mobile computing and networking*, pages 248–260, 2017.

[29] W. Mao, J. He, and L. Qiu. Acoustic motion tracking. In *Proc. of ACM MobiCom*, 2016.

[30] W. Mao, L. Qiu, J. He, Y. Cui, and S. Yun. Indoor follow me drone. In *Proc. of ACM MobiSys*, 2017.

[31] W. Mao, W. Sun, L. Qiu, S. Pradhan, and Y.-C. Chen. Room scale hand motion tracking. In *Proc. of ACM MobiCom*, 2019.

[32] W. Mao, W. Sun, M. Wang, and L. Qiu. Deeprange: Acoustic ranging via deep learning. *Proceedings of the ACM on Interactive, Mobile, Wearable and Ubiquitous Technologies*, 4(4):1–23, 2020.

[33] X. Meng, R. Liu, H. Chu, R. Peng, M. Wang, Y. Hao, and Y. Lai. Through-wall wireless communication enabled by a metalens. *Physical Review Applied*, 17(6):064027, 2022.

[34] H. Pan, L. Qiu, B. Ouyang, S. Zheng, Y. Zhang, Y.-C. Chen, and G. Xue. Pmsat: Optimizing passive metasurface for low earth orbit satellite communication. In *Proceedings of the 29th Annual International Conference on Mobile Computing and Networking*, pages 1–15, 2023.

[35] J. G. Proakis and M. Salehi. *Digital communications*, volume 4. McGraw-hill New York, 2001.

[36] S. Rallapalli, W. Dong, L. Qiu, and Y. Zhang. Waveloc: Wavelet signatures for ubiquitous localization. In *Proc. of IEEE MASS*, 2016.

[37] S. Rallapalli, W. Dong, L. Qiu, and Y. Zhang. Waveloc: Wavelet signatures for ubiquitous localization. In *2016 IEEE 13th International Conference on Mobile Ad Hoc and Sensor Systems (MASS)*, pages 219–227. IEEE, 2016.

[38] C. Rizos. Locata: A positioning system for indoor and outdoor applications where gnss does not work. In *Proceedings of the 18th Association of Public Authority Surveyors Conference*, pages 73–83. Citeseer, 2013.

[39] M. Rostami and K. Sundaresan. Enabling high accuracy pervasive tracking with ultra low power uwb tags. In *Proceedings of the 28th Annual International Conference on Mobile Computing And Networking*, pages 459–472, 2022.

[40] P. Roy and C. Chowdhury. A survey on ubiquitous wifi-based indoor localization system for smartphone users from implementation perspectives. *CCF Transactions on Pervasive Computing and Interaction*, 4(3):298–318, 2022.

[41] D. Song, P. fei Zhang, G. chao Fan, and C. dong Xu. An algorithm of selecting more than four satellites from gnss. In *2013 International Conference on Advanced Computer Science and Electronics Information (ICACSEI 2013)*, pages 134–138. Atlantis Press, 2013.

[42] E. Steindl, W. Dunkel, A. Hornbostel, C. Hättich, and P. Remi. The impact of interference caused by gps repeaters on gnss receivers and services. In *European Navigation Conference*, 2013.

[43] K. P. Subbu, B. Gozick, and R. Dantu. Locateme: Magnetic-fields-based indoor localization using smartphones. *ACM Transactions on Intelligent Systems and Technology (TIST)*, 4(4):1–27, 2013.

[44] Wikipedia. Beidou, 2024.

[45] Wikipedia. Galileo (satellite navigation), 2024.

[46] Wikipedia. Global positioning system, 2024.

[47] Wikipedia. Glonass, 2024.

[48] Wikipedia. Indium tin oxide, 2024.

[49] H. Wu, Z. Mo, J. Tan, S. He, and S.-H. G. Chan. Efficient indoor localization based on geomagnetism. *ACM Transactions on Sensor Networks (TOSN)*, 15(4):1–25, 2019.

[50] H. Xu, D. Wang, R. Zhao, and Q. Zhang. Faho: Deep learning enhanced holographic localization for rfid tags. In *Proceedings of the 17th Conference on Embedded Networked Sensor Systems*, pages 351–363, 2019.

[51] Z. Yang, W. Zeyu, J. Zhang, C. Huang, and Q. Zhang. Polarization-based visible light positioning. *IEEE Transactions on Mobile Computing*, 18(3):715–727, 2018.

[52] J. Yu, P. Wang, T. Koike-Akino, and P. V. Orlik. Multi-modal recurrent fusion for indoor localization. In *ICASSP 2022-2022 IEEE International Conference on Acoustics, Speech and Signal Processing (ICASSP)*, pages 5083–5087. IEEE, 2022.

[53] S. Yun, Y.-C. Chen, and L. Qiu. Turning a mobile device into a mouse in the air. In *Proc. of ACM MobiSys*, 2015.

[54] S. Yun, Y.-C. Chen, H. Zheng, L. Qiu, and W. Mao. Strata: Fine-grained acoustic-based device-free tracking. In *Proceedings of the 15th annual international conference on mobile systems, applications, and services*, pages 15–28, 2017.

[55] J. Zhang, C. Zhang, X. Zhang, and S. Banerjee. Towards a visible light network architecture for continuous communication and localization. In *Proceedings of the 3rd Workshop on Visible Light Communication Systems*, pages 49–54, 2016.

[56] M. Zhao, T. Chang, A. Arun, R. Ayyalasomayajula, C. Zhang, and D. Bharadia. Uloc: Low-power, scalable and cm-accurate uwb-tag localization and tracking for indoor applications. *Proceedings of the ACM on Interactive, Mobile, Wearable and Ubiquitous Technologies*, 5(3):1–31, 2021.